




For none, one, or two polarities—How do POLO junctions fit best into industrial Si solar cells?

Robby Peibst^{1,2}  | Christian Kruse¹ | Sören Schäfer¹ | Verena Mertens¹ |
 Stefan Bordihn¹  | Thorsten Dullweber¹ | Felix Haase¹ | Christina Hollemann¹ |
 Bianca Lim¹ | Byungsul Min¹ | Raphael Niepelt¹ | Henning Schulte-Huxel¹  |
 Rolf Brendel^{1,3}

¹Institute for Solar Energy Research Hamelin (ISFH), Emmerthal, Germany

²Institute of Electronic Materials and Devices, Leibniz Universität Hannover, Hannover, Germany

³Department of Solar Energy, Institute for Solid-State Physics, Leibniz Universität Hannover, Hannover, Germany

Correspondence

Robby Peibst, Institute for Solar Energy Research Hamelin (ISFH), Am Ohrberg 1, 31860 Emmerthal, Germany.
 Email: r.peibst@isfh.de

Funding information

German Federal Ministry for Economic Affairs and Energy, Grant/Award Number: FKZ 0324274B

Abstract

We present a systematic study on the benefit of the implementation of poly-Si on oxide (POLO) or related junctions into p-type industrial Si solar cells as compared with the benchmark of Passivated Emitter and Rear Cell (PERC). We assess three aspects: (a) the simulated efficiency potential of representative structures with POLO junctions for none (=PERC+), one, and for two polarities; (b) possible lean process flows for their fabrication; and (c) experimental results on major building blocks. Synergistic efficiency gain analysis reveals that the exclusive suppression of the contact recombination for one polarity by POLO only yields moderate efficiency improvements between 0.23%_{abs} and 0.41%_{abs} as compared with PERC+ because of the remaining recombination paths. This problem is solved in a structure that includes POLO junctions for both polarities (POLO²), for whose realization we propose a lean process flow, and for which we experimentally demonstrate the most important building blocks. However, two experimental challenges—alignment tolerances and screen-print metallization of p+ poly-Si—are unsolved so far and reduced the efficiency of the “real” POLO² cell as compared with an idealized scenario. As an intermediate step, we therefore work on a POLO IBC cell with POLO junctions for one polarity. It avoids the abovementioned challenges of the POLO² structure, can be realized within a lean process flow, and has an efficiency benefit of 1.59%_{abs} as compared with PERC—because not only contact recombination is suppressed but also the entire phosphorus emitter is replaced by an n+ POLO junction.

KEYWORDS

efficiency potential, passivating contacts, POLO, poly-Si, solar cell development

This is an open access article under the terms of the Creative Commons Attribution-NonCommercial License, which permits use, distribution and reproduction in any medium, provided the original work is properly cited and is not used for commercial purposes.

© 2019 The Authors. Progress in Photovoltaics: Research and Applications published by John Wiley & Sons Ltd.

1 | INTRODUCTION

The evolutionary improvement of Passivated Emitter and Rear (PERC or PERC⁺) solar cells poses a tough benchmark for the implementation of alternative concepts. Median production efficiencies have been increased almost linearly with approximately 0.5% per year, reaching now values well above 22%.² Recently, PERC record efficiencies of 24.1%³ and 24.4%⁴ have been announced. Although no details are disclosed so far and calibrated measurements according to ISO 17025/IEC 6094 are pending, these impressive results seem to provide a post-priori verification of a former controversially discussed simulation-based prediction of an efficiency potential for PERC beyond 24%.⁵ Besides efficiency improvements, further contributions to the continuous reduction of costs per Watt peak are the increase of throughput to up to 6000 wafers per hour and per front-end tool⁶ and an increase in wafer size. When implementing new technologies, the throughput has to be maintained, and any increase in process complexity has to be counterbalanced by a significant gain in efficiency.

On the other hand, it does not seem trivial to close the gap between current production median and record efficiencies for “conventional” PERC, and many groups work on conceptual improvements. There is strong industry interest in the implementation of passivating contacts. In particular, poly-Si on oxide (POLO) and related junction schemes, which can be implemented as a drop-in upgrade for the current technology, are already in pilot line production.⁷ Passivating contacts have proven their capability for efficiencies of at least 26.1% on lab-type IBC solar cells with POLO junction for both polarities⁸ and of at least 25.8% on lab-type double side contacted (DSC) cells with poly-Si on the rear and lab-type “conventional” selectively doped boron c-Si front side emitter.⁹ Nevertheless, their implementation in industrial solar cells is still a subject of ongoing research at many institutes and companies. The challenge is twofold—first, to transfer the high efficiency from the lab cells to the industrial scale and second, to reduce the process complexity down to a level that is competitive with the abovementioned PERC benchmark.

It is not clear yet which cell concept with passivating contacts (and which corresponding process flow) is most suited to address these challenges. Many groups are working on different cell concepts. Clearly, the “most prominent” cell structure with passivating contacts is an n-type cell with boron front emitter (including “unpassivated” front contacts) and n+ poly-Si on the rear, denoted as “TOPCon”,^{10,11} “monoPoly”,¹² “PaCo”,¹³ PERPoly,¹⁴ and so forth. Recently, an ISO 17025/IEC 6094 calibrated record efficiency of 24.6% has been announced¹⁵ for this structure on a large area cell. Other groups, too, reported excellent results of 23%,¹⁶ 24.2%,¹⁷ and 24.6%.⁴ This progress is particularly remarkable since it indicates that the limitation implied by the “unpassivated” screen-printed front side contact on the first industrial PERPoly cells¹⁴ has been mitigated. There is no information so far whether this improvement is achieved within an industrially feasible process flow. Addressing the “leaky bucket problem” by implementing passivating contacts for both polarities has proven its viability (efficiency-wise) on lab-type and industrial IBC cells.^{8,18,19} However, a lean process flow remains challenging for this approach because of the necessity of structuring. Nevertheless, also for DSC cell structures with

passivating contacts for only one polarity, the process complexity might cover a broad spectrum from potentially small (eg, by using firing-only contacts^{20,21}) to rather large.¹²

The aim of this work is therefore to provide a systematic study on the efficiency potential and process complexity of different representative cell structures with passivating contacts for one and for two polarities, and to compare it with the PERC benchmark without any passivating contacts. Since a potential process flow can be easily written on paper but can have drawbacks and road blockers in reality, we also address the main building blocks experimentally.

2 | APPROACH

2.1 | Choice of cell structures and process flows

The numbers of potential cell structures with passivating contacts and the number of potential process flows for their realization is huge. A systematic simulation-based comparison of the efficiency potential for (almost) all cell structures with passivating contacts will be published elsewhere.²² Here, we restrict ourselves to a limited number of representative examples to discuss the advantages and disadvantages of none vs one vs two passivating contact polarities.

For this and future works,²² we want to use the following notation: cell structures with passivating contacts for one polarity are denoted as “POLO” and cell structures with passivating contacts for two polarities are denoted as “POLO².” As prefix, we may write—if necessary in the specific context—the doping type of the substrate (n-Si or p-Si) and, in braces, the doping type of the poly-Si ({n} or {p}). As suffix, we may write the location of the pn-junction, which can also be formed between the “conventional polarity” and the wafer (front junction [FJ], back junction [BJ], or IBC). Other properties of the cell structures, such as the presence or absence of a front side diffusion or locally structured poly-Si, will be remarked in the text.

According to this system, the full notation of our 26.1% cell⁸ would be “p-Si POLO² IBC.” The full notation of a TOPCon/monoPoly/PaCo/PERPoly cell structure would be “n-Si {n}POLO FJ” (we would like to remark that we do not want to promote a further name here, but only to illustrate the logic of our notation system). While this notation would be systematic, it is quite lengthy and not catchy. If possible, we therefore try to simplify it and to define more “intuitive” names for the most important structures.

Figure 1 shows the schematic drawings of the cell structures selected for this study. All of the chosen exemplary structures utilize p-type bulk material, which has the lion's share of the market of more than 90% today. The structure representing the case without passivating contacts—and the ultimate benchmark—is the PERC+ cell.²³ From this starting point, first, we introduce passivating contacts for one polarity. There are two options to do so: putting n+ poly-Si locally under the metal fingers on the front side (p-Si {n}POLO FJ, here denoted as “PERC+ POLO”), or replacing the conventional Al₂O₃/SiN_x + Al-BSF rear side by p+ poly-Si (p-Si {p}POLO FJ).²⁴ It is also possible to replace the P-doped emitter completely with n+ poly-Si.

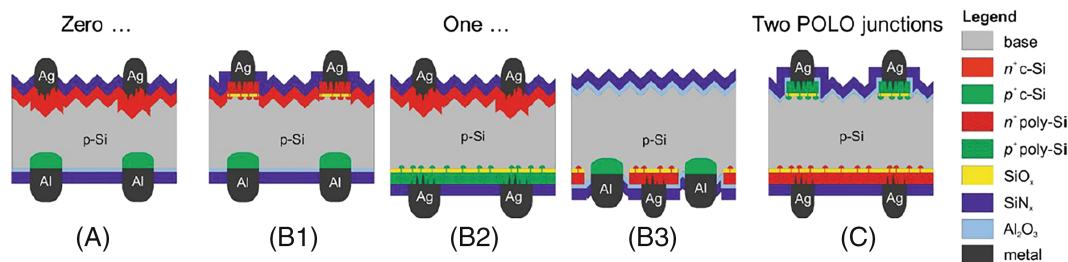


FIGURE 1 Schematic drawing—not to scale—of the cell structures investigated in this work with POLO junctions for (A) zero, (B1–3) one, and (C) two polarities. We use the following denotation: (A) PERC+, (B1) p-Si {n}POLO FJ = “PERC+ POLO,” (B2) p-Si {p}POLO FJ, (B3) p-Si {n} POLO IBC = “POLO IBC,” (C) p-Si POLO² BJ [Colour figure can be viewed at wileyonlinelibrary.com]

However, because of the strong parasitic absorption, the poly-Si then has to be located on the rear-side. One option to realize such a structure is an IBC cell with n+ POLO emitter, but still local Al BSF regions (p-Si {n}POLO IBC,^{25–28} here denoted as “POLO IBC”). For DSC structures with passivating contacts for two polarities, there are even more possibilities.^{29,30} We exemplarily chose—because of its high efficiency potential and potential lean process flow (see below)—a p-type cell with n+ poly-Si on the entire rear side and p+ poly-Si locally under the metal fingers on the front (p-Si POLO² BJ). We consider the specific case that no heavily diffused c-Si is present on the front. A similar structure, but with a “conventionally boron-doped local front surface field,” was proposed by Richter et al,⁹ and by Brendel et al²⁵ with a local front surface field formed by Al alloying.

For the envisaged process sequences, we restrict ourselves to options based on low-pressure chemical vapor deposition (LPCVD) of poly-Si. This implies that we not only have to deal with the double side deposition nature of LPCVD for the structures with poly-Si for one polarity, but that it also offers a very elegant way to realize the p-Si POLO² BJ structure with poly-Si for two polarities (see below). We also restrict ourselves to process options based on quartz furnace anneals for the POLO junction formation (i.e., we do not consider so far the firing-only^{20,21} approach). We acknowledge that there are further nominally single-sided deposition methods for Si such as the plasma-enhanced chemical vapor deposition,^{13,31–36} atmospheric-pressure chemical vapor deposition,²¹ sputtering,³⁷ electron beam evaporation,³⁸ and printing of liquid silicon.³⁹ These alternatives possibly enable not only different but also elegant process flows. However, most of our experimental evaluation of building blocks so far is based on LPCVD.

2.2 | Numerical device simulations

For the assessment of the efficiency potential and to generate an understanding of its limitations, we conduct numerical device simulations. The optical generation profiles are calculated by raytracing simulations using the SunRays software⁴⁰ and experimental n, k data for the poly-Si.^{41,42} The electrical simulations are based on the Quokka2 implementation⁴³ of the CoBo model⁴⁴ and the synergistic efficiency gain analysis (SEGA).^{45,46} The input parameters are listed in Table 1. A detailed discussion of them will be included in an upcoming publication.²²

Briefly summarized, we mainly use values measured in-house on test structures. Only if own measurement data is missing for a certain quantity, we use the best literature data available. Although we think that our in-house measurement data is consistent with recent publications from other groups, it therefore could be that slightly better values have been reported elsewhere (eg, for the properties of Ag on n+-doped c-Si textured surface). Also, we would like to remark that while many quantities are continuously improving, we had to freeze the input parameters at a certain point in time. One example is the J_0 value for fired Al₂O₃/SiN_x on planar surfaces, which we experimentally improved to 1 fA/cm² after the finalization of the manuscript. Nevertheless, such small changes do not affect the major conclusions of this work. As a last remark, we also want to point out that there are of course uncertainties in the measurement. To account for them in a simulation study, a sensitivity analysis would be required. However, with respect to the high number of cell structures investigated here, this seems to be not feasible. We would also not expect a significant effect on the results for realistic parameter ranges.

Our first priority for the simulation study is comparability of the different cell structures. We therefore assume the same base resistivity (0.9 Ω cm), the same respective bulk lifetime (as measured on a boron-doped p-type Czochralski-grown [Cz] wafer at ISFH after deactivation of the BO complexes), and the same finger pitches, metallized area fractions, etc. One should note that the latter parameters could be slightly optimized for each structure. In contrast to Min et al,⁵ we exclusively consider screen-print metallization (no plating). For metallized poly-Si regions, we assume the same passivation quality as achieved in the nonmetallized regions. In the face of the impressive progress in contacting poly-Si with firing-through screen printing,⁴⁷ multiple screen-printed poly-Si cells with open-circuit voltage values above 700 mV,^{17,18} and our own recent results, this seems a justified medium term assumption—at least for thick (approximately 200 nm) n-type poly-Si. For p-type poly-Si, maintaining the passivation quality after Ag/Al print is much more challenging (see, eg, Mack et al⁴⁸ and our own results below). We discuss the implication of an increased $J_{0,met,p+poly}$ in detail below. For the cell structures with local poly-Si regions underneath the metal fingers on the front, we take into account the necessity of alignment tolerances. According to our proposed process sequences, this implies that 200 nm thick poly-Si layers on planar surfaces remain in 22.5-μm-wide regions adjacent on both sides of the metal finger. The corresponding increase in reflection

TABLE 1 Main input parameters used for the SEGA simulation in this work.

Quantity	Value	Origin
Bulk		
Resistivity	0.9 Ω cm	measured at ISFH on 0.9 Ω cm B-doped Cz-Si after BO deactivation
τ_{no}	20 000 μ s	
τ_{po}	2000 μ s	
Wafer thickness	160 μ m	Typical value
Surfaces (non-contacted)		
Al ₂ O ₃ /SiN _x fired, planar surfaces	6 fA/cm ²	Measured at ISFH
Al ₂ O ₃ /SiN _x fired, textured surfaces	3 fA/cm ²	Measured at ISFH
Passivated P emitter, inter-finger regions	20 fA/cm ² ; 120 Ω /sq.	Extrapolated from current status at ISFH
Passivated P emitter, highly doped regions	100 fA/cm ² ; 95 Ω /sq.	Extrapolated from current status at ISFH
n+ poly-Si/SiN _x , non-metallized regions, planar surface	3 fA/cm ² ; 45 Ω /sq.	Measured at ISFH
p+ poly-Si/SiN _x , non-metallized regions, planar surface	5 fA/cm ² ; 150 Ω /sq.	Measured at ISFH
Contacts		
Ag on n+ doped c-Si, textured surface, laser doped from PSG	1850 fA/cm ² , 1.5 m Ω cm ²	Measured at ISFH
Ag on n+ poly-Si, planar surface	J_0 as on noncontacted regions; 1.5 m Ω cm ²	No lifetime reduction upon metallization resolvable, ρ_c measured at ISFH
Ag (Al) on p+ poly-Si, planar surface	J_0 as on noncontacted regions; 5 m Ω cm ²	Assumption, discussion see text
Al-BSF	500 fA/cm ² ; 3 m Ω cm ²	Measured at ISFH
Geometrical		
Ag and Ag/Al finger width	30 μ m	Extrapolated from current status at ISFH
Poly-Si finger width	75 μ m	Ambitious but potentially achievable alignment tolerances
Finger pitch front	1350 μ m	Typical values
Finger pitch rear	700 μ m	
IBC finger pitch	500 μ m	

and parasitic absorption is included in our area-weighted ray tracing simulations for the different regions of the cell.

How to experimentally combine all of these input parameters on one cell remains an open question. One example that this transfer might not always be straightforward is the SRH bulk lifetime in boron-doped Cz material, which is apparently lower on cell level than on test structures.⁴⁹ We also have to remark that Quokka2 is not capable to take into account the junction resistance between poly-Si and c-Si. However, since this resistance is very small for good junctions,^{50,51} the error implied by this constraint should be small.

2.3 | Proposed process flows using LPCVD

Table 2 shows a typical process flow for the PERC+ benchmark and our envisaged process flows for the structure with POLO junctions for one polarity (PERC+ POLO) and for the structure with POLO junctions for two polarities (p-Si POLO² BJ). For the process flow for the POLO IBC cell, we would like to refer the reader to Haase et al.²⁸ For a potential process flow for the p-Si {p}POLO FJ cell, we think that

the sequence reported in Duttagupta et al.¹² for the n-Si {n}POLO FJ cell is representative when switching all polarities.

To our knowledge, there is no common definition of how to count process steps and their combination. As a rule of thumb, we combine single steps if they can be performed subsequently in the same tool.

The process flow for PERC+ includes a selectively doped emitter (realized by laser doping from the phosphorus silica glass [PSG]). An ex situ thermal oxidation after PSG removal would add an additional step and change the order of steps if the oxide is not thin enough to stay underneath the Al₂O₃/SiN_x passivation on the rear.

For the integration of POLO junctions for one polarity, the process complexity might increase significantly.¹² Even for the realization of our PERC+ POLO cell, which has—except for the poly-Si underneath the metal fingers on the front—a very similar structure as the PERC+ cell, we have to add at least three process steps: (a) poly-Si deposition full area; (b) laser oxidation, ie, formation of a thin SiO_x by local heating of the finger regions; and (c) poly-Si removal in the interfinger regions via etching, where the SiO_x serves as etch mask.²⁵ If one would rather apply a full area poly-Si deposition, print an etch mask,

TABLE 2 Process flows for exemplary cell structures with zero, one and two POLO junctions

None PERC+	One PERC+ POLO	Two polarities passivating contacts p-Si POLO ² BJ
Preclean, texturization, clean	Preclean, texturization, clean, wet chemical oxidation	SDE, cleaning, wet chemical oxidation
POCl ₃ diffusion	Double-sided deposition of Si (LPCVD)	<i>Double-sided deposition of in situ p⁺-doped Si (LPCVD)</i>
Laser doping SE from PSG	<i>Laser oxidation finger regions front</i>	<i>Laser ablation inter-finger regions front</i>
Rear-side polishing, PSG removal, cleaning	<i>Diluted KOH, cleaning</i>	<i>Texturization, cleaning</i>
SiN _x front	POCl ₃ diffusion	<i>PECVD diffusion barrier front</i>
Al ₂ O ₃ /SiN _x rear	Rear-side polishing, PSG removal, cleaning	<i>POCl₃ diffusion incl. POLO junction formation and overcomp. rear</i>
LCO	SiN _x front	PSG and dielectric etch
Ag screen-print rear (solder pads)	Al ₂ O ₃ /SiN _x rear	Al ₂ O ₃ /SiN _x front
Al screen-print rear	LCO	SiN _x rear
Ag screen-print front	Ag screen-print rear (solder pads)	<i>Ag/Al screen-print front</i>
Co-firing	Al screen-print rear	Ag screen-print rear
	Ag screen-print front	<i>Co-firing</i>
	Co-firing	

Note. All process sequences refer to an LPCVD-based poly-Si deposition and a POLO junction formation via tube furnace anneal. Process steps which need to be developed are written in italic letters. Most of them are evaluated in the experimental section.

structure the poly-Si by wet chemical etching, and subsequently remove the mask, one would even add four process steps. One has to remark that the laser doping from the PSG, as necessary for the fabrication of the PERC+ cell, is not necessary for the PERC+ POLO cell. Thus, the net additional number of process steps is two (laser oxidation) or three (printed etch masks).

The integration of POLO junctions for two polarities does not necessarily increase the process complexity further (see Table 2). Our envisaged process flow for the p-Si POLO² BJ cell is quite lean: utilizing the chemical resistance of highly p-type-doped (greater than 10²⁰ cm⁻³) Si⁵² in alkaline etching solutions as an in situ-deposited etch mask turns the weakness of the double-sided LPCVD deposition into a strength. Laser ablation of the p+-type poly-Si in the interfinger regions and subsequent etching restricts the poly-Si to the finger regions on the front (+ alignment tolerances for screen print metallization). Laser machining of large areas is possible with high throughput with advanced laser techniques such as rotating polygon scanners.⁵³ The n-type doping of the poly-Si on the rear is realized by overcompensation of boron by phosphorus during POCl₃ diffusion. The high P diffusion coefficient in poly-Si, which is approximately four orders of magnitude larger than in monocrystalline Si,⁵⁴ should ensure that overcompensation is also possible for standard POCl₃ diffusions. LPCVD has the advantage of being capable of depositing thicker poly-Si layers (approximately 200 nm) without any blistering issues. Thus, sufficient lateral conductivity of the grid-contacted rear-side emitter can be ensured, and screen print metallization is facilitated. The dielectric stack on the rear serves as a rear-side reflector, as well as a source of atomic H for a hydrogenation of the n+-type POLO junction during firing. While pure SiN_x might be sufficient as well, the benefit of Al₂O₃/SiN_x stack as a hydrogen source has been demonstrated.⁵⁵ We therefore consider the Al₂O₃ layer on the rear as optional.

We also would like to remark that the proposed process sequence—with only slight modifications—could be applied for the realization of different POLO² cell structures. Starting with a p-type wafer, it yields a p-Si POLO²-BJ cell. Flipping the diffusion barrier to the rear, a p-Si POLO²-FJ cell with a P-doped c-Si emitter in the interfinger regions would be formed. Starting with an n-type wafer and also flipping the diffusion barrier to the rear would yield an n-Si POLO²-BJ cell with a P-doped c-Si front surface field in the interfinger regions. One could also apply the overcompensation approach for the fabrication of POLO² IBC cells.

A drawback of the proposed structure is that the Ag/Al front metallization of the hole collecting contact (p+ poly-Si) in our p-Si POLO²-BJ cell will possibly consume more Ag than the conventional rear-side of a PERC(+) cell, where Ag is only included in the soldering pads. This is a general issue of all cells without an Al metallization for one polarity.

2.4 | Experimental evaluation of essential building blocks

We evaluate the main building blocks for the proposed process sequences for the PERC+ POLO and p-Si POLO² BJ cell (Table 2) on test structures.

The full-area poly-Si deposition requires a structuring process that results in a selective removal of the poly-Si in the interfinger regions while leaving the poly-Si in the finger regions intact. The option we include in our proposed process sequence for the PERC+ POLO cell is the local laser oxidation. First, results on the experimental evaluation of this building block are reported below.

The most innovative process steps in our proposed process sequence for the p-Si POLO² BJ cell are the overcompensation of the boron

doping on one side of the wafer by phosphorus and the utilization of the etch resistance of p+-doped Si as an etch mask. Also, contacting the p-type poly-Si by screen print has been reported to be challenging.⁴⁸ All of these three building blocks are evaluated experimentally.

2.4.1 | Building blocks for the PERC+ POLO cell (laser oxidation finger regions front, diluted KOH, cleaning)

To develop this process, we use texturized p-type Cz silicon wafers with $1.5 \Omega \text{ cm}$ -base resistivity and M2 format. Using an E2000 LPCVD furnace from Centrotherm, we deposit 190 nm in situ n-type-doped Si on top of a wet chemically grown SiO_2 layer with a thickness (as determined by ellipsometry) of 1.7 nm.

Local laser oxidation is performed via UV-ps pulses with varying pulse energy and spot distance. Subsequently, the poly-Si is removed in the nonoxidized regions by etching in 20% KOH.

2.4.2 | Building blocks for the p-Si POLO² BJ cell#1 (Deposition of in situ p+-doped poly-Si)

To develop these processes, we use M2 n-type Cz wafers with a base resistivity of $2.7 \Omega \text{ cm}$ (after high temperature treatment). These wafers are damage-etched and cleaned within an RCA cleaning sequence. Subsequently, we grow wet-chemically an (DI/O_3) interfacial oxide with a thickness of $1.7 \pm 0.2 \text{ nm}$ as determined by ellipsometry. Next, we deposit 100 nm (group A) and 200 nm (group B) in situ p+-doped poly-Si on both sides in an E2000 LPCVD furnace from Centrotherm. For most of the samples, the POLO junction formation is performed in a quartz tube for 30 minutes in 900°C in nitrogen atmosphere. After junction formation, the samples are coated with 100 nm SiN_x and fired in a conveyor belt oven (DO-FF-8.600-300 from Centrotherm) in air. The samples approach the peak set fired temperature for a few seconds.

2.4.3 | Building blocks for the p-Si POLO² BJ cell#2 (laser ablation inter-finger regions, texturization, cleaning)

In order to investigate the local poly-Si removal by laser and subsequent wet chemical etching, we ablate on some of the test structures the poly-Si with a picosecond pulse laser at wavelength of 355 nm. We ablate $1.5 \times 1.5\text{-cm}^2$ sized regions on both sides of the test structures. Subsequently, we etch for varied etching times in 10% KOH at 75°C to remove the laser damage. Next, a texturization step is performed. We investigate the integrity of the p+ poly-Si etching barrier in the nonlaser-treated regions by scanning electron microscopy. In order to evaluate to what extent the laser damage is removed, we passivate the samples by SiN_x (2.4 refractive index). We use the dynamic infrared lifetime mapping method⁵⁶ (ILM) to assess the effective lifetime in the laser-treated regions.

2.4.4 | Building blocks for the p-Si POLO² BJ cell#3 (POCl₃ diffusion incl. overcompensation of p-type doping)

Samples dedicated to the test of the overcompensation concept are annealed in a standard POCl_3 diffusion. In order to supply atomic hydrogen to the c-Si/ SiO_x interface, we deposit 50 nm of SiN_x (refractive index of 2.05) by PECVD directly after junction formation (no HF dip). We perform photoconductance decay measurements prior to and after firing. The saturation current density of the POLO junctions in the nonmetallized regions is determined by the method of Kane and Swanson.⁵⁷ Doping profiles are measured by electrochemical capacitance voltage (ECV) measurements.

2.4.5 | Building blocks for the p-Si POLO² BJ cell#4 (Ag/Al screen-print on p+ doped poly-Si)

For screen printing, we test two different pastes: paste A, specifically designed for contacting p-poly; and paste B, designed for contacting p + c-Si emitters. We use a special test screen with finger openings of $50 \mu\text{m}$, separated in four quarters that have finger pitches of $P = \infty$, 350, 500, and $900 \mu\text{m}$. Printing on the rear therefore results in metallization fractions f_{met} of 0%, 5.6%, 10%, and 14.3%. In order to increase the aspect ratio and to avoid finger interruptions, we perform print-on-print. The firing set temperatures are split between 800°C , 830°C , 860°C , and 890°C .

We determine the saturation current density of the POLO junctions in the metallized regions via injection-dependent

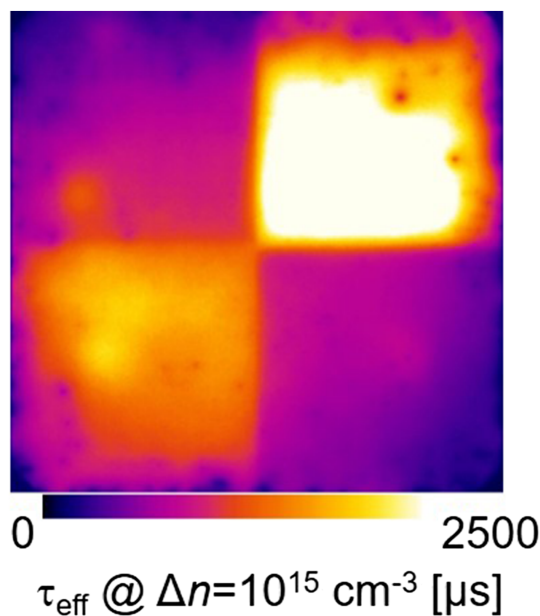


FIGURE 2 Photoconductance-calibrated photoluminescence image of a single-side metallized test structure, showing the effective lifetime τ_{eff} at an excess carrier density of 10^{15} cm^{-3} . In clockwise direction, starting from the upper left quarter, the metallization fractions are $f_{\text{met}} = 10\%$, 0% , 14.3% , and 5.6% . The nonmetallized quarter is used for calibration via contactless photoconductance [Colour figure can be viewed at wileyonlinelibrary.com]

photoconductance-calibrated photoluminescence lifetime imaging (PC-PLI) measurements, with a short-pass filter as described in Müller et al.⁵⁸ Figure 2 exemplarily shows a photoluminescence image for paste A, firing set temperature 860°C, and poly-Si thickness 200 nm.

$J_{0,\text{poly,met}}$ is determined as follows. First, we fit the injection-dependent effective lifetime of the nonmetallized quarter by accounting for the intrinsic lifetime limit,^{59,60} and using the SRH-capture time constant τ_{p0} , the symmetry factor $k = \tau_{\text{n0}}/\tau_{\text{p0}}$ and the saturation current density for recombination at the p-poly-passivated surface, $J_{0,\text{poly}}$, as fit parameters. We assume a single defect in the center of the bandgap. The so-determined τ_{p0} and k are then used to fit τ_{eff} for the remaining quarters with $J_{0,\text{surf}}$ as the only fit parameter. $J_{0,\text{poly,met}}$ then follows from $J_{0,\text{surf}} = (1 - f_{\text{met}}) J_{0,\text{poly}} + f_{\text{met}} J_{0,\text{poly,met}}$. We determine the specific contact resistance of the poly-Si/metal contact by the transfer length method (TLM).

3 | RESULTS AND DISCUSSION

3.1 | Simulation A—Idealized assumptions

Table 3 lists the simulated IV parameters for our exemplary cell structures with zero, one, and two polarities passivating contacts (compare Figure 1). Figure 3 shows the efficiency gains achievable by a hypothetic complete suppression of the respective recombination path according to SEGA.⁴⁵ An equivalent interpretation of the single bars is as a loss as compared with zero recombination (“loss_{acrzr}”) for the specific recombination path.

The PERC+ benchmark without POLO junctions has, for the input parameters chosen here (compare Table 1), an efficiency potential of 23.41%. This is lower than the 24.2% as simulated by Min et al.⁵ One of the main reasons for this difference is that in Min et al.,⁵ 10- μm -thin contact lines on the front (potentially realizable by plating) have been assumed, which reduces optical shading and the contact area fraction (front contact recombination). By contrast, we assume here 30- μm -wide screen-printed fingers with a much larger area of the metal/Si interface. The open-circuit voltage V_{oc} of the PERC+ cell is calculated to 688 mV. Figure 3 shows that the major limitation for V_{oc} is contact recombination at the emitter/front-grid interface, accounting for an efficiency loss of 0.47%_{abs}, as compared with zero contact recombination. Our in-house measured $J_{0,\text{met}}$ value of 1850 fA/cm² might be reduced in the future by better pastes or an optimization of the laser doping process, but it seems difficult to reduce it by an order of magnitude. Remarkably, recombination in the passivated emitter regions (0.3%_{abs} loss_{acrzr}) and the contact recombination at the hole contact on the rear (0.28%_{abs} loss_{acrzr}) are almost as large as the loss_{acrzr} because of front-contact recombination. Bulk recombination—as calculated based on our experimental value of $\tau_{\text{n0}} = 2000 \mu\text{s}$ measured after deactivation of the BO complexes—plays a minor role (0.07%_{abs} loss_{acrzr}). This impressively shows the recent progress achieved in boron-doped p-type Cz wafer material quality, which obviously does not pose an efficiency limitation and is therefore still competitive with n-type material. The short circuit current density J_{sc} of the PERC+ cell is 41.15 mA/cm². It is the highest of all DSC-simulated structures investigated here. In all other DSC cell

TABLE 3 Main IV parameters of the cell structures shown in Figure 1, simulated with the input parameters listed in Table 1

	None PERC+	One			Two polarities passivating contacts p-Si POLO ² BJ
		PERC+ POLO	p-Si {p}POLO FJ	POLO-IBC	
η , %	23.41	23.82	23.64	25.0	24.98
V_{oc} , mv	687.94	704.33	695.11	722.17	739.90
J_{sc} , mA/cm ²	41.15	40.92	41.01	41.49	40.62
FF, %	82.70	82.64	82.92	83.43	83.11

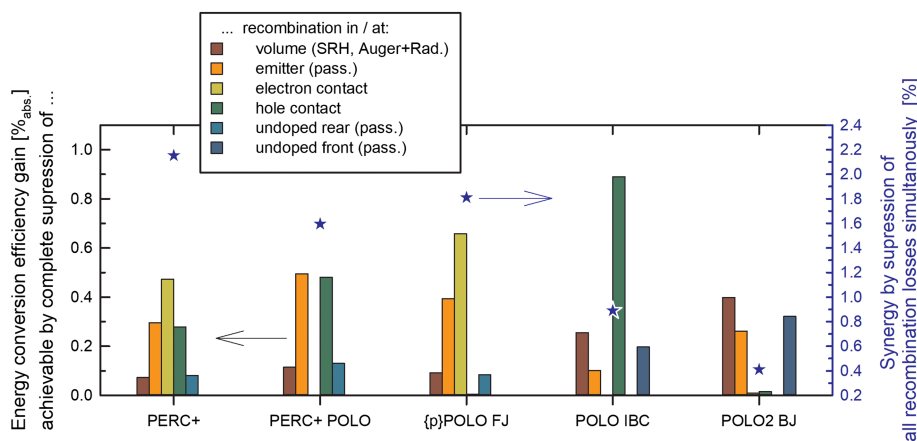


FIGURE 3 Left axis: energy conversion efficiency gains hypothetically achievable by complete suppression of recombination (main paths), calculated with SEGA for the cell structures shown in Figure 1. Right axis: efficiency gains due to synergy induced by a hypothetic simultaneous suppression of all recombination paths [Colour figure can be viewed at wileyonlinelibrary.com]

structures with at least one passivating contact, J_{sc} is reduced by parasitic absorption in the poly-Si. The fill factor of the PERC+ cell of 82.70% is limited by various series resistance contributions. Among them, the resistance implied by the lateral transport of majority carriers (holes) is a minor one and only accounts for an efficiency loss of 0.07%_{abs} as compared with zero hole transport resistance. Thus, the possibility to ensure a “one-dimensional current flow” by a full-area carrier collection on the rear is—at least for low-resistive base material as considered here—not a strong argument for the implementation of passivating contacts.

The PERC+ POLO structure addresses the main recombination loss by introducing n+ POLO junctions below the metal fingers on the front. This eliminates almost completely the corresponding efficiency loss_{aczf} (Figure 3). On the other hand, the remaining recombination losses_{aczf} are increased because of the leaky bucket principle. In particular, the recombination losses_{aczf} in the passivated emitter regions and recombination losses_{aczf} at the hole contact at the rear are both increased by 0.2%_{abs}. Thus, the resulting increase in V_{oc} from PERC+ to PERC+ POLO is moderate (16.3 mV). On the other hand, J_{sc} is reduced by 0.23 mA/cm² because of parasitic absorption and increased reflection at the poly-Si adjacent to the metal fingers. One should note that for less ambitious alignment tolerances, the reduction in J_{sc} (as compared with PERC+) is even more pronounced. Consequently, the increase in efficiency from PERC+ to PERC+ POLO of 0.41%_{abs} is decent, especially when set against the increase in process complexity (Table 2).

The leaky bucket principle also applies, of course, to the p-Si {p} POLO FJ cell. Here, the contact recombination at the rear is suppressed, but the other three main recombination paths, in particular the recombination at the electron contact on the front, are increased. Since the latter is already the major loss mechanism in the PERC+ cell, the V_{oc} of 695 mV is smaller than that of the PERC+ POLO cell. The reduction in J_{sc} (as compared with PERC+) is smaller in the p-Si {p} POLO FJ cell (0.14 mA/cm²) than in the PERC+ POLO cell, which shows that parasitic absorption in the poly-Si on the rear might be acceptable if it is overcompensated by other benefits. As mentioned above, the increase in fill factor because of the substitution of the conventional PERC+ rear side—local Al BSFs as “islands” in the passivated regions—by a full area collecting passivating contact is small (0.22%). The overall efficiency benefit of the p-Si {p} POLO FJ cell as compared with PERC+ is only 0.23%_{abs}. Although not chosen as an example in Table 2, the process flow for such a p-Si {p} POLO FJ cell, if based on LPCVD and tube furnace anneal, is complex.¹²

The POLO IBC cell also features a passivating contact only for one polarity. Nevertheless, it has, within the structures investigated here, an unique feature; compared with a PERC+ cell, it does not only address one recombination path (electron contact recombination as in the case of PERC+ POLO or hole contact recombination as in the case of p-Si {p} POLO FJ). Rather, the entire P-doped emitter in the c-Si, also in the passivated regions, is replaced by a well-passivating n+ POLO junction. Thus, the leaky bucket problem is addressed more effectively than in the former structures, and the resulting V_{oc} of 722 mV is much larger. This is the main reason for the high-efficiency potential of 25%, which is 1.59%_{abs} larger than for the PERC+ cell. The

remaining one of the former “big three” recombination paths in a PERC+ cell, the hole contact recombination, is increased to a loss_{aczf} of 0.89%_{abs} in the POLO IBC cell. The increase in fill factor also contributes to the increase in η for the POLO IBC cell. Besides the effect of different geometrical dimensions on the series resistance, the higher injection level at maximum power point—leading to a larger fraction of Auger recombination and thus to a higher pseudo fill factor—also implies an increased fill factor. The shortcircuit current density of the POLO IBC cell is increased by 0.34 mA/cm² as compared with that of the PERC+ cell, obviously because of the absence of front grid shading. However, it is worth mentioning that from simple geometric arguments (2.2% metal area fraction on front), one would expect a much higher increase in J_{sc} of 0.91 mA/cm². Since, as discussed above for the p-Si {p} POLO FJ cell, parasitic absorption in the poly-Si on the rear only accounts for approximately 0.14 mA/cm², the remaining gap of 0.43 mA/cm² is lost due to recombination. Under J_{sc} conditions, recombination at the high-low junctions (front-surface field, back-surface field) is most effective.⁶¹ Assuming that we will be able to transfer the excellent front-side passivation of 3 fA/cm² from test structures to our cells, the hole contact would imply the largest recombination loss even under J_{sc} conditions.

The p-Si POLO² BJ cell is, in this picture, a conceptual continuation. Here, all of the “big three” recombination paths in a PERC+ cell—electron and hole contact as well as emitter recombination—are addressed. Consequently, its V_{oc} of 739.9 mV is the highest of all cell structures investigated here. On the other hand, its J_{sc} of 40.62 mA/cm² is the lowest. Both parasitic absorption (reflection) in (at) the poly-Si on the front and parasitic absorption in the poly-Si on the rear are occurring here. Consequently, the efficiency potential of the p-Si POLO² BJ cell of 24.98% is on par with that of the POLO IBC cell. When compared

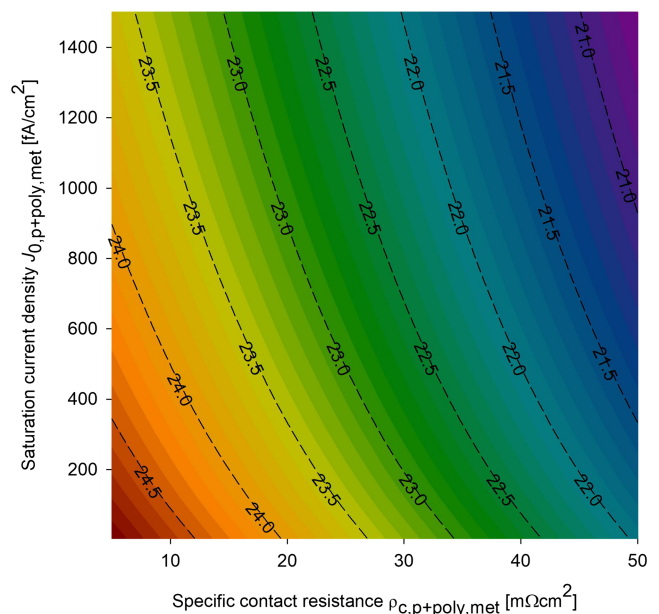


FIGURE 4 Contour-plot of the efficiency of the p-Si POLO² BJ cell for various combinations of $J_{0,p+poly,met}$, $\rho_{c,p+poly,met}$. The lower-left corner represents the value discussed above for “idealized assumptions” [Colour figure can be viewed at wileyonlinelibrary.com]

with the latter, the p-Si POLO² BJ might have the advantage of the applicability of conventional cell interconnection schemes.

It is remarkable that the sum of the single selected recombination losses_{ac,zr}, as calculated with SEGA, does not decrease from the PERC+ to the p-Si POLO² BJ structure. The increase in efficiency (in V_{oc}) from left to right in Figures 2 and 3 is rather implied by the decrease of the synergy induced by an simultaneous suppression of all recombination losses (right-hand axis of Figure 3).

3.2 | Simulation B—Technological constraints

One should note that for the simulations discussed above, a successful contacting of the p+ poly-Si without any degradation of the passivation quality are assumed. As shown by others⁴⁸ and confirmed by our own results of this work (see below), in particular the latter is, in practice, a so far unsolved challenge. At least for firing-through Ag/Al pastes, a good contact resistance can only be achieved at the price of a strong degradation of the passivation quality of the p+ POLO junctions in the metallized regions.

In order to quantify the effect of an increased $J_{0,p+poly,met}$ on the efficiency potential of the p-Si POLO² BJ cell, we vary $J_{0,p+poly,met}$

from 5 fA/cm² (equal to $J_{0,p+poly,pass}$) to 1500 fA/cm². The specific contact resistance ρ_c is varied from 5 to 50 m Ω cm². All other parameters are kept constant as specified in Table 2. Figure 4 shows the resulting contour plot for the efficiency. When comparing it with the experimental $J_{0,p+poly,met}$, $\rho_{c,p+poly,met}$ values (see below), it becomes obvious that the Ag/Al/p+-poly-Si contact has to be improved so that a p-Si POLO² BJ cell (or any cell with p+ POLO junctions, e.g., the p-Si {p}POLO FJ cell or our record p-Si POLO² IBC cell) can exploit its full efficiency potential.

3.3 | Experimental results on essential building blocks

In the following, we report on the results obtained so far for the building blocks marked in Table 2, based on the experimental approaches described in the previous section.

3.3.1 | PERC+ POLO cell (laser oxidation finger regions front, diluted KOH, cleaning)

Figure 5 shows scanning electron microscope (SEM) micrographs of the cross-section of locally laser-oxidized samples. While the poly-Si

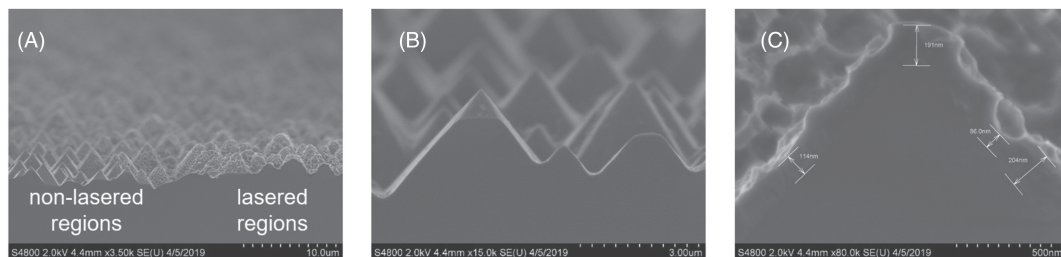


FIGURE 5 Scanning electron microscope (SEM) images of the cross-section of a locally laser-oxidized sample after poly-Si removal in the nonlasered interfinger regions in KOH. A, overview, B, larger magnification of the nonlasered interfinger regions where the poly-Si is successfully removed, C, larger magnification of the lasered finger regions where the poly-Si is roughened but successfully masked in the KOH step

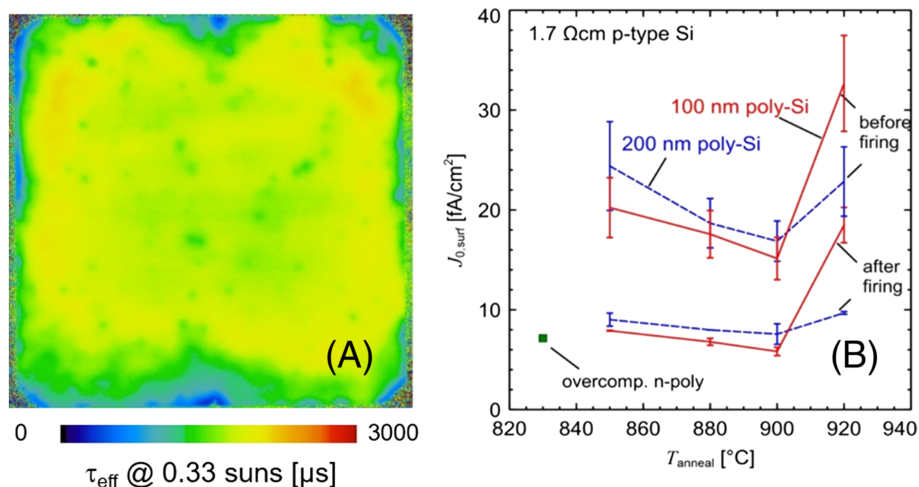


FIGURE 6 A, Dynamic Infrared Lifetime Map (ILM) image of an M2 Cz wafer with in situ p-type-doped low-pressure chemical vapor deposition (LPCVD) poly-Si after junction formation, B, J_0 values for the {p}POLO junctions with 100 and 200 nm poly-Si thickness before and after firing. The overcompensated n POLO junctions exhibit a J_0 value of 3 fA/cm² after SiN_x deposition before firing [Colour figure can be viewed at wileyonlinelibrary.com]

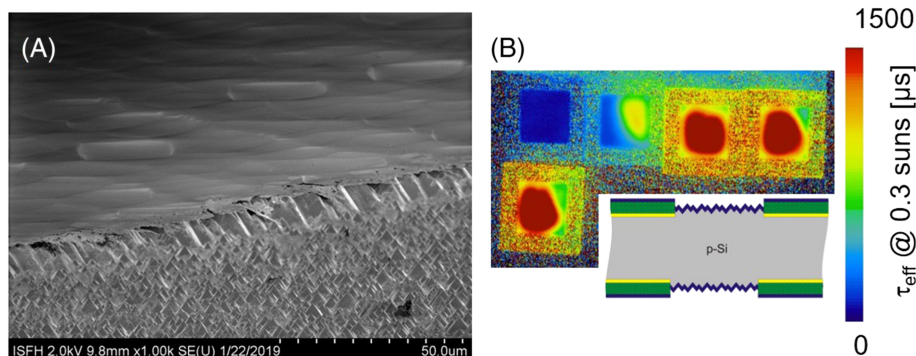


FIGURE 7 A, Scanning electron microscope (SEM) image of the edge between interfinger regions where the p+-poly-Si was laser-ablated prior to the texturization process, and the finger-regions where the p+-poly-Si was utilized as etch mask. B, Dynamic Infrared Lifetime Map (ILM) image of symmetric test structures (as sketched on the lower right) after laser ablation, KOH etch, texturization, and passivation. The different samples are KOH-etched for 0, 30, 60, 90, and 120 seconds, starting from the upper left sample to the right and ending at the sample in the second row [Colour figure can be viewed at wileyonlinelibrary.com]

in the nonlasered region is removed during the KOH etching (see Figure 5B), the lasered regions are protected by a thin SiO_2 .⁶²⁻⁶⁴ The remaining poly-Si is roughened and has a thickness between 90 and 190 nm, but nevertheless is still intact (see Figure 5C).

3.3.2 | p-Si POLO² BJ cell#1 (Deposition of in-situ p-doped poly-Si)

Figure 6A shows a Dynamic Infrared Lifetime Map (ILM) image of an M2 Cz wafer symmetrical lifetime sample with in situ doped poly-Si junctions after an annealing step at 900°C, giving an impression of the homogeneity of the surface passivation. Also, across the boat in the LPCVD tube, we obtain a good wafer-to-wafer homogeneity after an optimization of the in situ p-type-doped poly-Si deposition process.⁶⁵ Figure 6B shows the dependence of the surface recombination parameter $J_{0,\text{poly}}$ on the annealing temperature. The values before firing refer to the case directly after high-temperature anneal, the values after firing refer to the case after SiN_x deposition and firing at 850°C set temperature. For the optimum annealing temperature of 900°C, $J_{0,\text{poly}}$ takes a value of 5 fA/cm².

3.3.3 | p-Si POLO² BJ cell#2 (laser ablation inter-finger regions, texturization, cleaning)

Figure 7A shows an SEM image (tilted view) of a sample that has been locally laser-ablated, etched in 20% KOH for 120 seconds and subsequently texturized. The non-ablated p-poly-Si remains intact and withstands the wet chemical etching. Figure 7B shows ILM images at a photon flux equivalent to 0.3 suns. The samples from left to right and from top to bottom are etched for 0, 30, 60, 90, and 120 seconds in KOH prior to texturization. The results indicate that the texturization step itself is insufficient to remove the laser damage and that an additional KOH step of at least 60 seconds should be included in the process flow. The p-poly-Si region at the rim is in this case not surface-passivating, since it has not yet passed a high temperature annealing step at this stage.

3.3.4 | p-Si POLO² BJ cell#3 (POCl₃ diffusion incl. overcompensation of p-type doping)

Figure 8 shows an electrochemical capacitance-voltage (ECV) profile of the completely overcompensated poly-Si junction. No buried p-type doped layer is observed after a 100- Ω/\square POCl₃ diffusion. The green square symbol in Figure 6B refers to the $J_{0,\text{poly}}$ of the overcompensated n-poly Si surface after SiN_x deposition and firing. This value increases from 3 fA/cm² from before firing to 8 fA/cm² after firing.

3.3.5 | p-Si POLO² BJ cell#4 (Ag/Al screen-print on p+ doped poly-Si)

Figure 9 shows the results of the fire-through paste evaluation on p-poly-Si. The SiN_x layer used here has a thickness of 50 nm. The metal

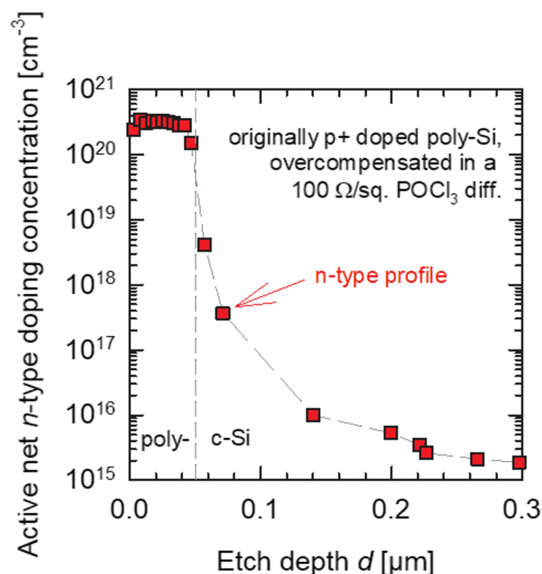


FIGURE 8 Electrochemical capacitance voltage (ECV) profile of an n POLO junction after overcompensation of originally p+-type-doped poly-Si in a 100- Ω/sq POCl₃ diffusion [Colour figure can be viewed at wileyonlinelibrary.com]

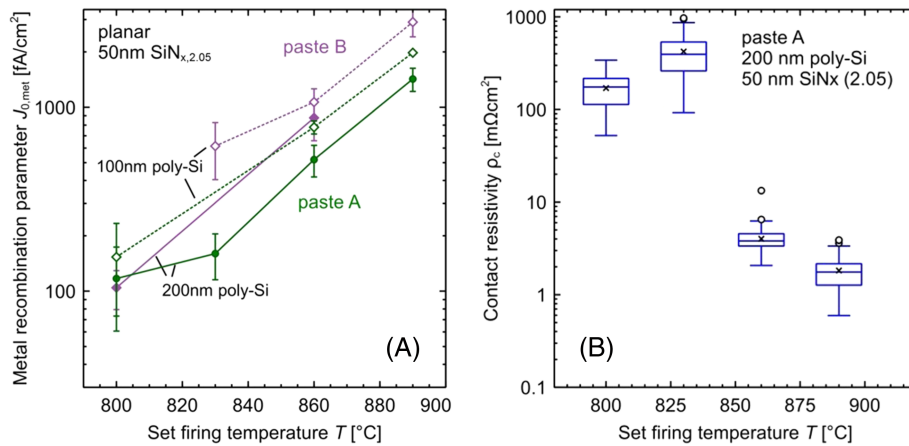


FIGURE 9 A, Saturation current density $J_{0,\text{p+poly,met}}$ in the metallized regions of the {p}POLO junctions as a function of firing set temperature for two different pastes A,B and two different poly-Si thicknesses. B, Specific metal/p+ poly-Si contact resistance for paste A and poly-Si thickness of 200 nm as a function of firing set temperature [Colour figure can be viewed at wileyonlinelibrary.com]

recombination parameter $J_{0,\text{p+poly,met}}$, plotted in Figure 9A for the two different pastes and two different poly-Si thicknesses, is the average value of the three quarters with varying f_{met} . Paste A results in slightly lower $J_{0,\text{p+poly,met}}$ values than paste B and ranges from $117 \pm 56 \text{ fA/cm}^2$ when fired at a set temperature of 800°C to $1470 \pm 220 \text{ fA/cm}^2$ when fired at 890°C . The 100-nm poly-Si layers show higher $J_{0,\text{p+poly,met}}$ values for the same paste and firing condition compared with the 200-nm poly-Si. The reason is that the fire-through paste locally penetrates the poly-Si layer more easily the thinner it gets. Figure 8B shows the corresponding contact resistivities between the paste and the poly-Si layer. Contact resistivities below $10 \text{ m}\Omega \text{ cm}^2$ are achieved only for set firing temperatures above 860°C . The results indicate that at this point, it seems to be difficult to maintain the passivating contact properties after screen printing with fire-through pastes. For the set firing temperatures investigated, 860°C yields the best contact properties (paste A, 200 nm poly-Si thickness). According to Figure 4, an efficiency of 24.1% would be achievable with a p-Si POLO² BJ cell with the measured $J_{0,\text{p+poly,met}}$ and $\rho_{0,\text{p+poly,met}}$ values (and the other parameters according to Table 1). This is a high value, but might be also achievable with nonpatterned devices featuring passivating contacts for one polarity on the rear. Pastes might be improved or alternative processes like combinations of laser contact openings and nonfiring through pastes⁸ might be applied in the future, so that the full benefit of passivating contacts for two polarities can be exploited.

3.4 | First cell results for the POLO IBC structure

For the POLO IBC structure, essentially all building blocks are in place. As reported in Haase et al,²⁸ we verify the findings of others⁴⁷ that state-of-the-art Ag pastes designed for contacting n+ poly-Si can simultaneously achieve low specific contact resistances and (almost) completely maintain the passivation quality of the POLO junctions in the metallized area if the firing temperature is carefully chosen. We also attempt to quantify the $J_{0,\text{n+poly,met}}$ value with the PC-PLI method

described previously. The puzzling observation was that the effective lifetimes in some metallized quarters of the test structures were actually higher than in the nonmetallized reference quarter. Thus, a reliable analysis of the $J_{0,\text{n+poly,met}}$ value—which should be positive—was not possible. We suspect that the real temperature during firing was different for the different quarters of the sample. This aspect requires further investigation. In Haase et al,²⁸ we report on 21.8% efficient POLO IBC structures (M2 wafers but active cell area 4 cm^2 , designated area, in-house measurements). Meanwhile, we have improved the efficiency to 22.6%. The main reasons for the discrepancy between these first experimental results and the simulated efficiency potential according to Table 3 were identified to be a nonwell-working front side recombination (greater than 30 fA/cm^2) and perimeter losses. Meanwhile, we have improved the passivation quality of fired $\text{Al}_2\text{O}_3/\text{SiN}_x$ stack down to the abovementioned value of 3 fA/cm^2 . We are currently applying this front-side passivation on the next cell batch, and we are expecting a significant efficiency improvement.

4 | CONCLUSION

We systematically compare different cell structures with passivating contacts for none, one, and two polarities. We consider the following aspects: (a) simulation-based efficiency potential calculation and identification of main loss channels based on a SEGA, (b) possible elegant process sequences for the realization of these cell structures, and (c) the experimental evaluation of essential building blocks of these sequences.

Regarding (a), we calculate a moderate increase in the efficiency potential when implementing one POLO junction in such a manner that only one of the main recombination paths of the PERC+ benchmark is addressed: 0.41% for the PERC+ POLO cell with n+ poly-Si below the metal fingers on the front side (electron contact recombination suppressed), and 0.23% for the p-Si {p}POLO FJ cell with p+ poly-Si on the rear (hole contact recombination suppressed). When implementing one POLO junction in such a manner that two major recombination paths of the PERC+ cell are addressed, the increase in the efficiency

potential is much larger. For the POLO IBC cell, the phosphorus-doped c-Si emitter is completely substituted by a well-passivating n+ POLO junction. Thus, electron contact recombination and recombination in the passivated emitter regions are mitigated. The simulated efficiency potential of the POLO IBC cell is 25%. Implementing POLO junctions for two polarities can furthermore suppress the recombination at the hole contact, implying even higher open-circuit voltages close to 740 mV for the p-Si POLO² BJ cell. However, for all DSC structures with local poly-Si (and metal) on the front, parasitic absorption in and reflection at the poly-Si fingers—wider than the metal fingers to provide alignment tolerances—decrease the short-circuit current density. Thus, the simulated efficiency potential for the p-Si POLO² BJ cell is “only” 24.98%. The J_{sc} decrease could be avoided by locating both POLO junctions (and the metal contacts) on the rear as on our record 26.1% efficient p-Si POLO² IBC cell.

Regarding (b) and (c), we propose to use local laser oxidation for the structuring of the poly-Si on the front of a PERC+ POLO cell. This approach limits the number of additional process steps to two (ie, one less than for straightforward print of a mask, etch-back, and mask removal). We demonstrate that with a picosecond laser at 355 nm, a thin oxide can be grown, which successfully masks the finger regions during poly-Si removal in the nonlasered inter-finger regions. Whether the passivation quality in the lasered finger regions is still maintained is subject of ongoing work.

In order to realize a p-Si POLO² BJ cell with poly-Si for both doping polarities, we propose here first to utilize the relatively small etch rate p+ poly-Si for structuring in alkaline solutions (no additional deposition of an etch barrier necessary), and an overcompensation of the original p+ doping by phosphorus on the rear side. This sequence would require only one LPCVD poly-Si deposition and one high temperature front-end step, yielding a process complexity comparable with that of the PERC+ benchmark. We successfully demonstrate the approach for structuring, ie, the complete removal of the laser damage in the interfinger regions and a sufficient integrity of the p+ poly-Si etch barrier during etching. We also successfully demonstrate that an overcompensation of the original p+ doping is possible within a standard 100-Ω/sq POCl₃ diffusion. The passivation quality of both POLO junctions—the in situ p-type-doped and the overcompensated n-type-doped—is excellent (3 to 7 fA/cm² after firing) and homogeneous across the wafer.

However, our results obtained so far for the evaluation of firing-through screen print metallization on p+ poly-Si show that it is currently hardly possible to maintain a good passivation quality in the metallized regions while achieving a low specific contact resistance. The current quality of these metal/p+ poly-Si contacts limits the efficiency potential of the p-Si POLO² BJ cell to 24.1%. The pastes might be improved or alternative processes like combinations of laser contact openings, and nonfiring through pastes⁸ might be applied in the future. By contrast, all building blocks for the POLO IBC cell seem to be in place already. With respect to the efficiency potential, lean-ness of the process flow, and the current technological constraints, this structure therefore seems to be an attractive intermediate step before implementing passivating contacts for both polarities.

ACKNOWLEDGEMENTS

We would like to thank Agnes Merkle for her contributions to the evaluation of screen-print metallization of p+ poly-Si and Audie Yeo and Boris Veith-Wolf for their contributions to the improvement of the Al₂O₃/SiN_x. We furthermore would like to thank Luise aus der Fünten for her help with TLM and PC-PLI measurements and L Menze for the optimization of in situ boron-doped and LPCVD-deposited polycrystalline Si. We would like to thank Larysa Mettner, Anja Mercker, Tobias Neubert, David Sylla, Ulrike Sonntag, Uwe Höhne, and Guido Glowatzki for sample processing. This work is funded by the German Federal Ministry for Economic Affairs and Energy under grant FKZ 0324274B (Genesis).

ORCID

Robby Peibst  <https://orcid.org/0000-0001-8769-9392>

Stefan Bordihn  <https://orcid.org/0000-0001-7077-7905>

Henning Schulte-Huxel  <https://orcid.org/0000-0003-4785-0080>

REFERENCES

- Dullweber T, Schulte-Huxel H, Blankemeyer S, et al. Present status and future perspectives of bifacial PERC+ solar cells and modules. *Jpn J Appl Phys*. 2018;57(8S3):08RA01.
- Lee BG, Höger I, Ballmann T, et al. *Development of p-Cz PERC solar cells approaching 23% efficiency for gigawatt-level production*, Proc. of the 35th EUPVSEC; 2018: 398.
- Press release from Longi solar from Jan. 16th 2019: <https://www.pv-tech.org/news/longi-solar-has-bifacial-mono-perc-solar-cell-world-record-verified-at-24.0>
- Press release from Jinko solar from June 3rd 2019 <https://www.pv-magazine.com/2019/06/03/jinkosolar-records-469-3-w-monocrystalline-module/>
- Min B, Müller M, Wagner H, et al. A roadmap toward 24% efficient PERC solar cells in industrial mass production. *IEEE J Photovolt*. 2017;7(6):1541.
- Chen Y, Altermatt PP, Chen D, et al. From laboratory to production: learning models of efficiency and manufacturing cost of industrial crystalline silicon and thin-film photovoltaic technologies. *IEEE J Photovolt*. 2018;8(6):1531.
- Chen Y. Presented at the PV-CellTech conference, Kuala Lumpur, Malaysia; 2019.
- Haase F, Hollemann C, Schäfer S, et al. Laser contact openings for local poly-Si-metal contacts enabling 26.1%-efficient POLO-IBC solar cells. *Solar Energy Mater Solar Cells*. 2018;186:184-193.
- Richter A, Benick J, Feldmann F, Fell A, Hermle M, Glunz SW. n-Type Si solar cells with passivating electron contact: identifying sources for efficiency limitations by wafer thickness and resistivity variation solar energy materials and solar cells. *Sol Energy Mater Sol Cells*. 2017;173:96-105.
- Feldmann F, Bivour M, Reichel C, Hermle M, Glunz SW. Passivated rear contacts for high-efficiency n-type Si solar cells providing high interface passivation quality and excellent transport characteristics. *Sol Energy Mater Sol Cells*. 2014;120:270-274.
- While this cell structure was first proposed by the ISE in 2013, the notation “Tunnel oxide passivated contact”(TOPCon) originally denoted a junction scheme with a thin interfacial oxide and a C-

- containing, partially crystalline Si layer with a higher bandgap than Si. It has now been generalized to this cell structure and all passivated contact schemes based on "poly-Si". Our scientific reasons for keeping our own notation "POLO" for this junction scheme (proposed at the same time) can be found in Peibst R, Römer U, Larionova Y, et al. Working principle of carrier selective poly-Si/c-Si junctions: is tunnelling the whole story? *Solar Energy Mater Solar Cells*. 2016;158:60-67.
12. Duttagupta S, Nandakumar N, Padhamnath P, Kitz Buatis J, Stangl R, Aberle AG. monoPoly cells: large-area crystalline silicon solar cells with fire-through screen printed contact to doped polysilicon surfaces. *Solar Energy Mater Solar Cells*. 2018;187:76-81.
 13. König M, Kluge T, Grosse T, et al. Single side passivated contact technology exceeding 22.5% with industrial production equipment, Proc. of the 7th WCPEC, 1000; 2018.
 14. Stodolny MK, Lenes M, Wu Y, et al. N-type polysilicon passivating contact for industrial bifacial n-type solar cells. *Solar Energy Mater Solar Cells*. 2016;158:24-28.
 15. Press release from Trina solar, May 28th 2019, <https://www.pv-tech.org/news/trina-solar-uses-super-sized-n-type-mono-wafer-for-record-24.58-i-topcon-bi>
 16. Nandakumar N, Rodriguez J, Kluge T, et al. Investigation of 23% monoPoly screen-printed silicon solar cells with an industrial rear passivated contact, Proc. of the 46th IEEE PVSC; 2019.
 17. Yang J. *Advanced technology exploration for c-Si solar cells at Jinko*, presented at the CSPV; 2018.
 18. Press release from Trina solar, Feb 14th 2018, <https://www.pv-tech.org/news/trina-solar-takes-n-type-mono-ibc-cell-to-record-25.04-conversion-efficiency>
 19. Bunea G. Presented at MRS fall meeting; 2018.
 20. Ingenito A, Nogay G, Jeangros Q, et al. A passivating contact for silicon solar cells formed during a single firing thermal annealing. *Nat Energy*. 2018;3:800-808.
 21. Merkle A, Seren S, Knauss H, et al. *Atmospheric pressure chemical vapor deposition of in-situ doped amorphous silicon layers for passivating contacts*, Proc. of the 35th EUPVSEC; 2018: 785-791.
 22. Kruse C, Brendel R. to be submitted; 2019.
 23. Dullweber T, Kranz C, Peibst R, et al. PERC+: Industrial PERC solar cells with rear Al grid enabling bifaciality and reduced Al paste consumption. *Prog Photovolt*. 2016;24(12):1487-1498.
 24. Feldmann F, Bivour M, Reichel C, Steinkemper H, Hermle M, Glunz SW. Tunnel oxide passivated contacts as an alternative to partial rear contacts. *Solar Energy Mater Solar Cells*. 2014;131:46-50.
 25. Brendel R, Kruse C, Merkle A, Schulte-Huxel H, Haase F, Peibst R. *Screening carrier selective contact combinations for novel crystalline Si cell structures*, Proc. of the 35th EUPVSEC; 2018: 39-46.
 26. Peibst R. *In-depth study of poly-Si /Oxide/c-Si junctions and p+ poly-Si/n+ poly-Si tunneling junctions for applications in Si single junction and Si-based tandem cells*, presented at the MRS fall meeting; 2019.
 27. Stodolny MK, Wu Y, Anker J, et al. *Review and outlook of doped and undoped LPCVD PolySi based passivating contacts for industrial Si solar cells*, SiliconPV conference; 2019.
 28. Haase F, Hollemann C, Schäfer S, Krügener J, Brendel R, Peibst R. *Transferring the record p-type Si POLO-IBC cell technology towards an industrial level*, Proc. of the 46th IEEE PVSC; 2019.
 29. Bronsveld P. *Upscaling passivating and carrier selective contacts for industrial applications*, presented at MRS fall meeting; 2018.
 30. Tous L. *Large-area industrial nPERT cells—status and perspectives*, presented at MRS fall meeting; 2018.
 31. Stuckelberger J, Nogay G, Wyss P, et al. Passivating electron contact based on highly crystalline nanostructured silicon oxide layers for silicon solar cells. *Sol En Mat Sol Cells*. 2016;158:2-10.
 32. Tao Y, Upadhyaya V, Chen C-W, et al. large area tunnel oxide passivated rear contact n-type Si solar cells with 21.2% efficiency. *Prog Photovolt: Res Appl*. 2016;24:830-835.
 33. Young DL, Nemeth W, LaSalvia V, et al. Interdigitated back passivated contact (IBPC) solar cells formed by ion implantation. *IEEE J Photovolt*. 2016;6:41.
 34. Feldmann F, Bivour M, Reichel C, Steinkemper H, Hermle M, Glunz SW. Tunnel oxide passivated contacts as an alternative to partial rear contacts. *Sol En Mat Sol Cells*. 2014;131:46-50.
 35. Steinhauser B, Polzin J-I, Feldmann F, Hermle M, Glunz SW. Excellent surface passivation quality on crystalline silicon using industrial scale direct-plasma topcon deposition technology. *Solar RRL*. 2018;2:1800068.
 36. Peibst R, Larionova Y, Reiter S, et al. *Implementation of n+ and p+ poly junctions on front and rear side of double-side contacted industrial silicon solar cells*, Proc. 32nd EUPVSEC; 2016: 323-327.
 37. Yan D, Cuevas A, Phang SP, Wan Y, Macdonald D. 23% efficient p-type crystalline silicon solar cells with hole-selective passivating contacts based on physical vapor deposition of doped silicon films. *Appl Phys Lett*. 2018;113:061603.
 38. Lossen J, Hoß J, Eisert S, et al. *Electron beam evaporation of silicon for poly-silicon/SiO₂ passivated contacts*, Proc of the 35th EUPVSEC; 2018: 418.
 39. Kiefer F. *Inkjet printing as a new method for the preparation of POLO contacts*, presented at the MRS fall meeting; 2018.
 40. Brendel R. *Sunrays: a versatile ray tracing program for the photovoltaic community*. Proc. of the 12th EUPVSEC; 1994.
 41. Min B, Vogt MR, Wietler T, et al. Increasing the photo-generated current in solar cells with passivating contacts by reducing the poly-Si deposition temperature. *AIP Conf Proc*. 2018;1999(1):040015.
 42. Reiter S, Koper N, Reineke-Koch R, et al. Parasitic absorption in polycrystalline Si-layers for carrier-selective front junctions. *Energy Procedia*. 2016;92:199-204.
 43. Fell A. A free and fast three-dimensional/two-dimensional solar cell simulator featuring conductive boundary and quasi-neutrality approximations. *IEEE Trans Elec Dev*. 2013;60:733-738.
 44. Brendel R. Modeling solar cells with the dopant-diffused layers treated as conductive boundaries. *Prog Photovolt*. 2012;20(1):31-43.
 45. Brendel R, Dullweber T, Peibst R, Kranz C, Merkle A, Walter D. Break-down of the efficiency gap to 29% based on experimental input data and modelling. *Prog Photovolt*. 2016;24(12):1475-1486.
 46. Kruse CN, Bothe K, Brendel R. Comparison of free energy loss analysis and synergistic efficiency gain analysis for PERC solar cells. *IEEE J Photovolt*. 2018;8(3):683-688.
 47. Padhamnath P, Wong J, Nagarajan B, et al. Metal contact recombination in monoPoly™ solar cells with screen-printed & fire-through contacts. *Sol En Mat Sol Cells*. 2019;192:109-116.
 48. Mack S, Schube J, Fellmeth T, Feldmann F, Lenes M, Luchies J-M. Metallisation of boron-doped polysilicon layers by screen printed silver pastes. *Phys Status Solidi RRL*. 2017;11(12):1700334.
 49. Lim B, Merkle A, Peibst R, Dullweber T, Wang Y, Zhou R. *LID-free PERC + solar cells with stable efficiencies up to 22.1%*, Proc. of the 35th EUPVSEC; 2018: 359-365.
 50. Rienäcker M, Bossmeyer M, Merkle A, et al. Junction resistivity of carrier-selective polysilicon on oxide junctions and its impact on solar cell performance. *IEEE J Photovolt*. 2017;7(1):11-18.

51. Kökbudak G, Müller R, Feldmann F, Fell A, Turan R, Glunz SW. *On the determination of the contact resistivity for passivating contacts using 3D simulations*, Proc. of the 33rd EUPVSEC; 2017: 242-246.
52. Steinsland E. Boron etch-stop in TMAH solutions. *Sens Act A*. 1996;54(1-3):728-732.
53. www.scanlab.de/en/products/advanced-scanning-solutions/polygon-scanner-systems
54. Split FHM, Bakke H. Diffusion of donor elements (125 Sb, 82 P, 74(73) As) in polycrystalline silicon. *Phys Stat Solidi A Appl Res*. 1986;97(1):135-142.
55. van de Loo B, Schnabel M, Stodolny M, et al. *On the hydrogenation of poly-Si passivating contacts by Al₂O₃ and SiN_x thin films*, Proc. of the 8th SiliconPV conference; 2018.
56. Ramspeck K, Reissenweber S, Schmidt J, Bothe K, Brendel R. Dynamic carrier lifetime imaging of silicon wafers using an infrared-camera-based approach. *Appl Phys Lett*. 2008;93(10):102104.
57. Kane DE, Swanson RM. *Measurement of the emitter saturation current by a contactless photoconductivity decay method*, Proc. of 18th IEEE PVSC; 1985: 578-583.
58. Müller J, Bothe K, Herlufsen S, Ohrdes T, Brendel R. Reverse saturation current density imaging of highly doped regions in silicon employing photoluminescence measurements. *IEEE J Photovolt*. 2012;2(4): 473-478.
59. Richter A, Glunz SW, Werner F, Schmidt J, Cuevas A. Improved quantitative description of Auger recombination in crystalline silicon. *Phys Rev B*. 2012;86:165202.
60. Veith-Wolf BA, Schäfer S, Brendel R, Schmidt J. Reassessment of intrinsic lifetime limit in n-type crystalline silicon and implication on maximum solar cell efficiency. *Solar Energy Mater Solar Cells*. 2018;186:194-199.
61. Ohrdes T, Römer U, Larionova Y, Peibst R, Altermatt PP, Harder N-P. *High fill-factors of back-junction solar cells without front surface field diffusion*, Proc. of the 27th EUPVSEC; 2012: 866-869.
62. Boyd IW, Wilson JIB, West JL. Laser-induced oxidation of silicon. *Thin Solid Films*. 1981;83(4):L173-L176.
63. Kailath BJ, DasGupta A, DasGupta N, Singh BN, Kukreja LM. Growth of ultra-thin SiO₂ by laser-induced oxidation. *Semicond Sci Tech*. 2009;24(10):105011.
64. Du Z, Zhang C, Li F, Zhou R, Hong M. Impact of laser-induced oxidation on silicon wafer solar cell" performance. *IEEE J Photovolt*. 2016;6(3):617-623.
65. Menze L. *Optimization of in situ boron-doped and LPCVD deposited polycrystalline Si*, Bachelor thesis, Leibniz University Hannover; 2018.

How to cite this article: Peibst R, Kruse C, Schäfer S, et al. For none, one, or two polarities—How do POLO junctions fit best into industrial Si solar cells? *Prog Photovolt Res Appl*. 2020;28:503-516. <https://doi.org/10.1002/pip.3201>